Large temperature coefficient of resistance in atomically thin two-dimensional semiconductors

Cite as: Appl. Phys. Lett. **116**, 203105 (2020); doi: 10.1063/5.0003312
Submitted: 31 January 2020 · Accepted: 1 May 2020 ·
Published Online: 19 May 2020

Asir Intisar Khan,[1] Pedram Khakbaz,[2] Kevin A. Brenner,[1] Kirby K. H. Smithe,[1] Michal J. Mleczko,[1] David Esseni,[2] and Eric Pop[1,3,a)]

AFFILIATIONS

[1]Department of Electrical Engineering, Stanford University, Stanford, California 94305, USA
[2]Dipartimento Politecnico di Ingegneria e Architettura, University of Udine, 33100 Udine, Italy
[3]Department of Materials Science and Engineering, Stanford University, Stanford, California 94305, USA

[a)]Author to whom correspondence should be addressed: epop@stanford.edu

ABSTRACT

The temperature coefficient of resistance (TCR) of thin metal lines is often used for applications in thermometry, bolometers, or thermal accelerometers. However, metal TCR is much degraded in nanometer-thin films due to strong surface scattering, preventing their use as fast thermal sensors, which simultaneously require low thermal mass and large TCR. In contrast, here we show that the TCR of doped two-dimensional (2D) semiconductors is large ($\sim$0.3% K^{-1} at 300 K in MoS_2 and $MoTe_2$) even at sub-nanometer thickness. This is larger than that of any metals with thicknesses up to $\sim$35 nm and larger than that of $\sim$95 nm thick Cu lines (0.25% K^{-1}) at 300 K. At 100 K, the TCR of these 2D materials is doubled, $\sim$0.6% K^{-1}. Comparison with detailed 2D transport models suggests that the TCR could be further enhanced (up to 0.45% K^{-1} at 300 K and $\sim$2.5% K^{-1} at 100 K) by reducing the density of Coulomb impurities and scattering centers. Such high TCR in atomically thin 2D semiconductors could lead to the design of fast thermal sensors.

Published under license by AIP Publishing. https://doi.org/10.1063/5.0003312

Temperature sensing is critical for several applications including nanoscale thermometry,[1,2] thermal accelerometers,[3,4] bolometers,[5] and suppression of thermal failures in integrated circuits.[6,7] Traditional temperature sensors rely on thermocouples, platinum or polysilicon resistors, or circuit-based sensors.[8,9] However, the former cannot be placed with microscale precision and most cannot respond to ultra-fast temperature transients.[7,9] Instead, their relatively large thermal masses make them slow to recognize sharp temperature changes and limit their potential performance.[10,11]

Fast thermal sensing requires a large temperature coefficient of resistance (TCR) as well as low thermal capacitance,[12] which can be obtained by thinning the sensor.[4,11] However, when thinned below $\sim$10 nm, the TCR of metals drops sharply due to strong surface scattering and possible electron localization, limiting their use as fast thermal sensors,[3,4,13] as further discussed below. In contrast, here we demonstrate that atomically thin 2D semiconductors such as MoS_2 and $MoTe_2$ maintain large TCRs, up to $\sim$0.3% K^{-1} at 300 K and $\sim$0.6% K^{-1} at 100 K, from sub-nanometer to few-nanometer thickness. This is significantly higher than the TCR of metals at sub-10 nm thickness (e.g., 0.08% K^{-1} for 3.7 nm Pt,[14] and 0.02% K^{-1} for 4.5 nm TiN,[15] at 300 K) and higher than the TCR of 95 nm thick Cu ($\sim$0.25% K^{-1} at 300 K or 0.52% K^{-1} at 100 K).[16] Fundamentally, and unlike in ultra-thin metals, phonon-limited transport in high-quality atomically thin 2D semiconductors maintains a large TCR, potentially enabling applications for fast temperature sensing.

We focus on measurements of monolayer MoS_2 (three atoms, or 0.615 nm thick) and $\sim$13 layer ($\sim$9.4 nm thick) $MoTe_2$ devices. These are selected as representative devices among numerous others fabricated and described elsewhere,[17–19] with the focus here being on TCR measurements and simulations. Figures 1(a) and (b) display schematics of the MoS_2 and $MoTe_2$ devices ($L = 3.6\ \mu$m and 1.02 μm, respectively) on SiO_2 (thickness $t_{ox} = 30$ nm). The highly doped Si substrates serve as back-gates to test the dependence on charge carrier density, i.e., doping. These devices are sufficiently long to have minimal contact resistance contribution, i.e., the measured contact resistance for the monolayer MoS_2 and multilayer $MoTe_2$ devices was $\sim$1.3 k$\Omega\cdot\mu$m and $\sim$2 k$\Omega\cdot\mu$m, respectively,[17,19] at room temperature and $\sim$$10^{13}$ cm^{-2} carrier density, accounting for $\sim$5% ($\sim$20%) of the total device resistance at 300 K (80 K). (The complete temperature dependence of contact resistance was reported in Refs. 17 and 19). All electrical measurements were in vacuum ($\sim$$10^{-5}$ Torr) after an *in situ* anneal at 250 °C, which improves contact resistance and minimizes hysteresis.

Published under license by AIP Publishing

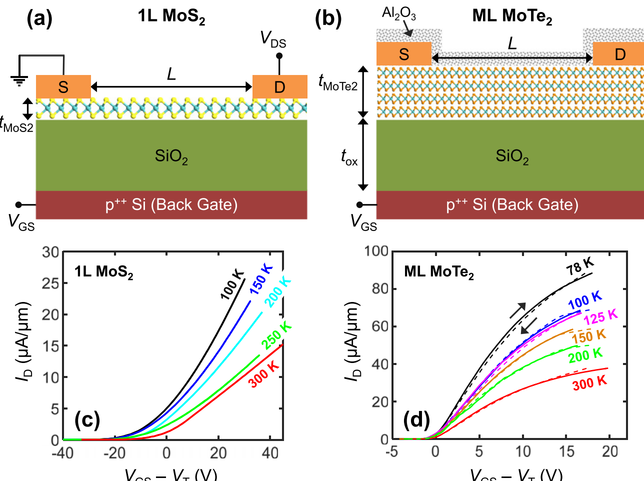

FIG. 1. (a) Schematic of the measured monolayer (1L) MoS_2 device, with Ag/Au contacts. (b) Schematic of the measured multilayer (ML) $MoTe_2$ device, encapsulated by Al_2O_3, with Ag contacts. Film thicknesses are $t_{MoS2} \approx 0.615$ nm (single layer) and $t_{MoTe2} \approx 9.4$ nm (13-layers), and both materials are in the 2H semiconducting phase. (c) Measured I_D normalized by width vs V_{GS} - V_T at several temperatures for MoS_2 and (d) for $MoTe_2$. The MoS_2 device has negligible hysteresis. The $MoTe_2$ device has small hysteresis, with arrows indicating the sweep direction of solid and dashed lines. All measurements are in vacuum. $V_{DS} = 0.1$ V and 1 V for Figs. 1(c) and 1(d), respectively.

Figures 1(c) and 1(d) display measured drain current (I_D) vs back-gate voltage adjusted by threshold voltage (V_{GS}–V_T), from 100 K to 300 K, revealing negligible hysteresis under forward and backward sweeps for the MoS_2 device, and a small amount of hysteresis for the $MoTe_2$ device. The drain bias (V_{DS}) was kept low to avoid self-heating. The resistance (R) was obtained for all temperatures at the same carrier density, $n \approx C_{ox}(V_{GS}–V_T)/e$, where $C_{ox} \approx 115$ nF/cm^2 is the measured capacitance[18] of the 30 nm SiO_2, and e is the elementary charge. TCR estimates are performed at relatively high n, from $\sim 7.2 \times 10^{12}$ cm^{-2} to $\sim 2.15 \times 10^{13}$ cm^{-2}, to ensure band-like transport and improve Coulomb or charged impurity (CI) screening.

Figures 2(a) and 2(b) depict the measured R vs temperature (T) for MoS_2 and $MoTe_2$, respectively, at several carrier densities, n. Error bars arise from the combined uncertainty of threshold voltage (V_T) estimates with three different methods (linear extrapolation, Y-function and second derivative[20]) and that of the (minimal) hysteresis seen in Fig. 1(d). TCRs were obtained by fitting lines to the experimental data, with $R = R_0[1 + \alpha(T - T_0)]$, where α is the TCR, T_0 is the initial T and R_0 is the average R at T_0, across all carrier densities tested. We note that $\alpha = (1/R_0)(dR/dT)$; thus by definition the TCR itself could be a function of temperature, depending on the reference temperature (T_0) at which the TCR is evaluated. Across the considered carrier densities, we find an average TCR (at $T_0 = 300$ K) of $\alpha = 0.27 \pm 0.01\%$ K^{-1} for monolayer MoS_2 and $\alpha = 0.28 \pm 0.02\%$ K^{-1} for 13-layer $MoTe_2$. With the reference temperature $T_0 = 100$ K, the estimated TCRs are $\alpha = 0.53 \pm 0.04\%$ K^{-1} and $0.63 \pm 0.01\%$ K^{-1} for monolayer MoS_2 and 13-layer $MoTe_2$, averaged across the carrier densities shown in Fig. 2.

The change of resistance with temperature in these 2D devices is attributed to their temperature-dependent mobility. The mobility is limited by scattering with intrinsic phonons (iPh), with surface optical phonons (SO Ph.) of the substrate, and with CIs, as further discussed below. The slightly higher TCR in the multi-layer $MoTe_2$ device (particularly at 100 K) can be attributed to the current flow being distributed further from the interface and CIs, enabling iPh to be more dominant compared to monolayer devices.[21,22] In Fig. 3(a), we replot the measured R at three temperatures vs carrier density n, and then we display the TCR vs n in Fig. 3(b) at $T_0 = 300$ K. TCR increases with n because CIs are more effectively screened by larger carrier densities, enabling a more phonon-dominated mobility. Based on Fig. 3(b), the maximum TCRs (at $T_0 = 300$ K) measured in this work were 0.28% K^{-1} for monolayer MoS_2 and 0.30% K^{-1} for 13-layer $MoTe_2$. At 100 K, the maximum TCRs measured were 0.57% K^{-1} and 0.64% K^{-1}, respectively.

To interpret the temperature dependence of resistance in the monolayer limit (MoS_2), we performed numerical simulations using the Linearized Boltzmann Transport Equation (LBTE). We included both conduction band valleys of MoS_2, K and Q,[23] and electron scattering with acoustic and optical phonons *intrinsic* to the MoS_2 (iPh), as well as remote SO phonons and CIs of the SiO_2 substrate, the latter two mechanisms describing the *extrinsic* effect of the substrate. Some scattering mechanisms involved were anisotropic (e.g., SO Ph. and CIs); thus, we did not introduce any of the isotropic simplifications often employed for the LBTE,[24] but instead performed a direct, numerical solution with the approach of Refs. 23 and 25.

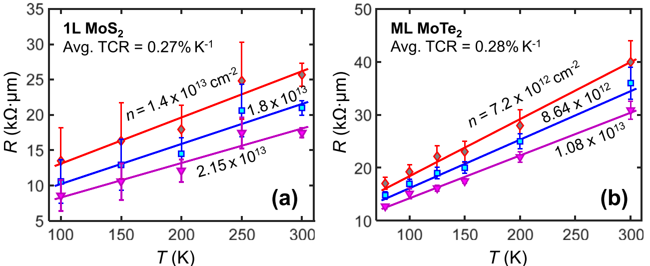

FIG. 2. Extracting the temperature coefficient of resistance (TCR) at several carrier densities n for (a) monolayer MoS_2 and (b) 13-layer $MoTe_2$. Symbols are measured resistance adjusted by the device width. Solid lines are fits vs temperature (T), whose slope indicates the TCR. The average TCRs listed on the plots are at $T_0 = 300$ K; at 100 K they are ≈2x larger (see text).

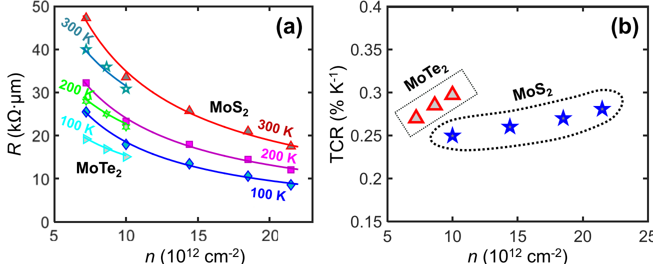

FIG. 3. (a) Measured resistance (adjusted by width) vs estimated carrier density n at different temperatures for MoS_2 and $MoTe_2$ devices. (b) Extracted TCR (at $T_0 = 300$ K) vs carrier density for our 2D material devices, here monolayer MoS_2 and 13-layer $MoTe_2$. The TCR of these 2D materials is as high as $\sim 0.6\%$ K^{-1} at $T_0 = 100$ K.

Published under license by AIP Publishing

The scattering models for intrinsic MoS_2 phonons, the deformation potentials, and the phonon energies are described in Refs. 23 and 26. The effective masses (m_t and m_l), band nonparabolicity factors (α_{np}), and K to Q valley offset ($\Delta E_{K\text{-}Q}$) were obtained from *ab initio* calculations,[26] shown in Table I, and the MoS_2 is assumed unstrained. SO Ph and CI scattering account for extrinsic effects of the SiO_2 substrate. For SO phonons, we consider only the SiO_2 transverse optical (TO) mode with the lowest energy $\hbar\omega_{TO} = 55.6$ meV, assuming semi-infinite SiO_2 and vacuum, respectively, below and above MoS_2, and neglecting the possible coupling between SiO_2 phonons and MoS_2 plasmons.[27] This allows us to write the secular equation $[\epsilon_{SiO_2}^{int} + (\epsilon_{SiO_2}^{0} - \epsilon_{SiO_2}^{int})/(1 - \omega^2/\omega_{TO}^2)] = \epsilon_0$ solving for $\omega = \omega_{SO}$.[23] For a static $\epsilon_{SiO_2}^{0} = 3.9\epsilon_0$ and an intermediate frequency SiO_2 dielectric constant $\epsilon_{SiO_2}^{int} = 3.05\epsilon_0$ (ϵ_0 being the permittivity of vacuum), we obtain $\hbar\omega_{SO} = 61$ meV. The matrix element for the SO phonon mode can thus be written as follows:[23]

$$M_{SO}\left(\vec{k},\vec{k}'\right) = \sqrt{\frac{\hbar\omega_{SO}}{2Aq}\left(\frac{1}{\epsilon_{SiO_2}^{int}+\epsilon_0} - \frac{1}{\epsilon_{SiO_2}^{0}+\epsilon_0}\right)}, \quad (1)$$

where $\vec{k}$ is the initial and $\vec{k}'$ is the final state, A is a normalization area in the transport plane, and $q = |\vec{k} - \vec{k}'|$. For CI scattering, the Fourier transform of the scattering potential energy produced by a charged impurity located at $(x, y, z) = (0, 0, z_0)$ is

$$\phi(q,z) = \frac{e^2}{2q\epsilon_{MoS_2}}\left[e^{-|z-z_0|} + Ce^{qz} + De^{-qz}\right], \quad (2)$$

where $0 < z < t_{MoS2}$ is inside the MoS_2 layer, and z_0 can be either in the MoS_2 layer or in the substrate. The coefficients C and D are given in Ref. 23 (with substitutions for the dielectric constants), $\epsilon_{MoS_2} = 7.6\epsilon_0$, and the matrix element can be calculated analytically. We also accounted for CI screening due to MoS_2 free carriers, according to the static dielectric function approach.[23]

Figure 4(a) reports the simulated mobility vs temperature showing the expected power law dependence ($\mu \propto T^{-\gamma}$) with an exponent varying between $\gamma = 1$ and 1.9 depending on the scattering mechanism included in the analysis. Figure 4(b) shows the calculated resistance $R = L/(en\mu)$ with $L = 3.6\,\mu$m (the length of measured MoS_2 sample) as a function of temperature. By neglecting CIs (bottom two curves), the simulations predict TCR as large as 0.45% K^{-1} at 300 K (~2.5% K^{-1} at $T_0 = 100$ K). In particular, green circles were obtained for iPh only; hence they correspond to a suspended MoS_2 with no scattering sources related to the SiO_2 substrate. By including an equivalent CI density $N_{imp} = 1.3 \times 10^{12}\ cm^{-2}$ (top three curves), the calculated room temperature resistance is in good agreement with experiments, the temperature dependence becomes weaker, and the TCR drops to ~0.34% K^{-1} at 300 K. Here, N_{imp} may be low compared

TABLE I. Parameters from DFT calculations for monolayer MoS_2, where m_0 is the free electron mass.

	K valley		Q valley		
$\Delta E_{K\text{-}Q}$	$m_t = m_l$	α_{np}	m_t	m_l	α_{np}
0.195 (eV)	0.47 (m_0)	0.94 $(eV)^{-1}$	0.54 (m_0)	1.14 (m_0)	1.16 $(eV)^{-1}$

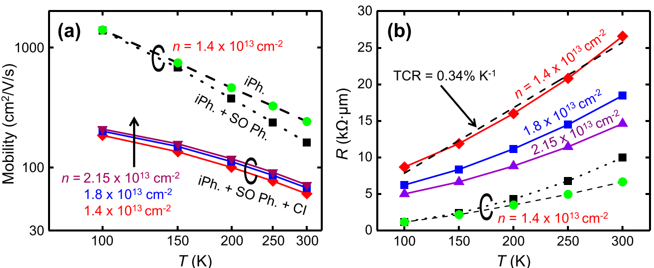

FIG. 4. Numerical simulations. (a) Monolayer MoS_2 mobility vs temperature for different carrier densities. Simulations are for different scattering mechanisms: intrinsic MoS_2 phonons (iPh), surface optical phonons of the SiO_2 substrate (SO Ph), and Coulomb impurities (CI). (b) Calculated resistance (adjusted by width) vs temperature for scattering mechanisms in (a) and $L = 3.6\,\mu$m, like the measured sample. CI density is $N_{imp} = 1.3 \times 10^{12}\ cm^{-2}$ for the top three simulations and $N_{imp} = 0$ for the bottom two. Dashes with TCR = 0.34% K^{-1} are a linear fit to the calculated resistance, which most closely matches the experiments at $T_0 = 300$ K.

to the measured sample, because it is an equivalent density of CIs in the middle of the MoS_2, where the matrix element for Coulomb scattering is the largest.[23,26]

The simulated TCR is slightly larger than the experimental value, which is mainly due to an overestimation of simulated mobility (i.e., underestimate of resistance) at $T = 100$ K. Uncertainty regarding the actual position and density of CIs can also explain the difference between simulations and experiments. Importantly, simulations suggest that the TCR of 2D materials could be improved by reducing the density of CIs.

The TCRs obtained here for ultra-thin 2D devices are significantly higher than those of ultra-thin metals, as shown in Fig. 5. For all TCR extractions we took $T_0 = 300$ K to make a consistent comparison. Although the TCRs measured for ultra-thin 2D devices are slightly lower than the TCR of bulk metals, the TCR for sub-nanometer thin monolayer MoS_2 is higher than that for 95 nm thick Cu lines (~0.25% K^{-1})[16] and significantly higher than the TCR of metals at comparable (i.e., sub-10 nm) thicknesses. We also note that

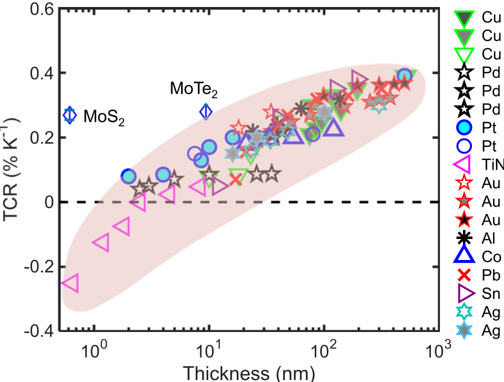

FIG. 5. Measured TCR vs material thickness. Our measured TCR values at 300 K for monolayer MoS_2 (0.615 nm thick) and multi-layer $MoTe_2$ (9.4 nm thick) are shown with blue diamonds. TCR data at 300 K for various metals (symbols in shaded region) have been extracted from the literature for Cu,[16,39,40] Pd,[41–43] Pt,[14,44] TiN,[15] Au,[45–47] Al,[41] Co, Ag,[40,41] Sn, and Pb.[48]

Published under license by AIP Publishing

metal TCRs decrease with film thickness and can even become negative in TiN films thinner than ∼3 nm.[15] The trends observed for thin metals are due to increased scattering by surface roughness and grain boundaries.[28,29] Few-nanometer thin metal films could even be discontinuous or oxidized, displaying negative TCR due to hopping-like transport between separated metal islands.[15,30] On the other hand, the large positive TCR of ultra-thin 2D devices illustrates that it is strongly influenced by phonon scattering, even in such atomically thin films. Moreover, our simulations suggest that 2D TCR could be further increased by reducing the density of Coulomb impurities.

While an in-depth discussion of potential applications is beyond the scope of this work, we point out that the large TCR of ultra-thin 2D devices could enable fast yet simple thermal sensors by overcoming the limitation of low TCR in thin metal lines. These would be thin bridge-like sensors, with the 2D material supported by a few-nanometer thin insulator (e.g., SiO_2 or Si_3N_4) and capped by few-nanometer thin suboxides for doping (e.g., AlO_x, TiO_x, or MoO_x).[31–33] Proper chemical doping eliminates the need for a back-gate, which was used here to test the carrier density dependence. The charge transfer doping separates the dopants (in the suboxide) from the mobile carriers (in the 2D material), thus preserving their mobility,[31–33] which could even be enhanced by dielectric or carrier screening.

Regarding the time response of such 2D sensors, molecular dynamics simulations have shown that the thermal time constant of a 2D material on a nanometer-thin oxide is only ∼0.1–0.4 ns,[34] significantly faster than the simulated response times of diode sensors (∼165 ns) in complementary metal-oxide-semiconductor (CMOS) silicon on insulator (SOI) technology.[35] While PIN diodes hold an advantage from the point of view of CMOS integration, this comes at the expense of a lower TCR (∼0.2% K^{-1} at 300 K)[36] and larger area.[35] Outside of CMOS, ultrathin 2D temperature sensors could be integrated into thermal interface materials (TIMs), where they would introduce a thermal interface resistance of only $\sim 10^{-4}$ cm^2K/W,[37] significantly lower than that of conventional TIMs, ∼0.1 cm^2K/W.[38]

In summary, we have demonstrated a large TCR in atomically thin 2D materials (∼0.3% K^{-1} at 300 K and ∼0.6% K^{-1} at 100 K), significantly higher than that of metals in the sub-10 nm-thickness range. Simulations show that even larger TCRs (up to 0.45% K^{-1} at 300 K and ∼2.5% K^{-1} at 100 K) in monolayer 2D devices could be obtained by further reducing the density of charged impurities. These could enable fast temperature sensors with low thermal resistance and thermal capacitance at the atomically thin limit.

This work was supported in part by the National Science Foundation (NSF) Engineering Research Center for Power Optimization of Electro-Thermal systems (POETS) with Cooperative Agreement No. EEC-1449548 and by the Stanford SystemX Alliance. K.A.B. acknowledges partial support from the Intelligence Community Postdoctoral Fellowship. P.K. and D.E. are thankful to Professor M. Pourfath and M. Hosseini for fruitful discussions.

REFERENCES

[1] C. D. S. Brites, P. P. Lima, N. J. O. Silva, A. Millán, V. S. Amaral, F. Palacio, and L. D. Carlos, Nanoscale **4**, 4799 (2012).
[2] D. Estrada, Z. Li, G.-M. Choi, S. N. Dunham, A. Serov, J. Lee, Y. Meng, F. Lian, N. C. Wang, A. Perez, R. T. Haasch, J.-M. Zuo, W. P. King, J. A. Rogers, D. G. Cahill, and E. Pop, npj 2D Mater. Appl. **3**, 10 (2019).
[3] C. L. M. Everhart, K. E. Kaplan, M. M. Winterkorn, H. Kwon, J. Provine, M. Asheghi, K. E. Goodson, F. B. Prinz, and T. W. Kenny, in IEEE Micro Electro Mechanical Systems (2018), pp. 976–979.
[4] F. Mailly, A. Giani, A. Martinez, R. Bonnot, P. Temple-Boyer, and A. Boyer, Sens. Actuators, A **103**, 359 (2003).
[5] F. Purkl, T. S. English, G. Yama, J. Provine, A. K. Samarao, A. Feyh, B. Kim, G. O'Brien, O. Ambacher, R. T. Howe, and T. W. Kenny, in *17th International Conference Solid-State Sensors, Actuators Microsystems, Transducers Eurosensors XXVII* (IEEE, 2013), pp. 1507–1510.
[6] A. Vassighi and M. Sachdev, IEEE Trans. Device Mater. Reliab. **6**, 300 (2006).
[7] N. Zhang, C. M. Lin, D. G. Senesky, and A. P. Pisano, Appl. Phys. Lett. **104**, 073504 (2014).
[8] W. Yang, H. Jiang, and Z. Wang, Sensors **19**, 1777 (2019).
[9] G. C. M. Meijer, *Smart Sensor Systems* (John Wiley & Sons, 2008), pp. 185–223.
[10] R. Mukherjee, J. Basu, P. Mandal, and P. K. Guha, J. Micromech. Microeng. **27**, 123002 (2017).
[11] S. K. Nam, J. K. Kim, S. C. Cho, and S. K. Lee, Sensors **10**, 6594 (2010).
[12] R. C. Webb, A. P. Bonifas, A. Behnaz, Y. Zhang, K. J. Yu, H. Cheng, M. Shi, Z. Bian, Z. Liu, Y. S. Kim, W. H. Yeo, J. S. Park, J. Song, Y. Li, Y. Huang, A. M. Gorbach, and J. A. Rogers, Nat. Mater. **12**, 938 (2013).
[13] C. H. Sharma, A. P. Surendran, A. Varghese, and M. Thalakulam, Sci. Rep. **8**, 12463 (2018).
[14] H. J. Kim, K. Kaplan, P. Schindler, S. Xu, M. M. Winterkorn, D. Heinz, T. English, J. Provine, F. B. Prinz, and T. W. Kenny, ACS Appl. Mater. Interfaces **11**, 9594 (2019).
[15] H. Van Bui, A. Y. Kovalgin, J. Schmitz, and R. A. M. Wolters, Appl. Phys. Lett. **103**, 051904 (2013).
[16] J. J. Plombon, E. Andideh, V. M. Dubin, and J. Maiz, Appl. Phys. Lett. **89**, 113124 (2006).
[17] K. K. H. Smithe, C. D. English, S. V. Suryavanshi, and E. Pop, Nano Lett. **18**, 4516 (2018).
[18] K. K. H. Smithe, S. V. Suryavanshi, M. Muñoz Rojo, A. D. Tedjarati, and E. Pop, ACS Nano **11**, 8456 (2017).
[19] M. J. Mleczko, A. C. Yu, C. M. Smyth, V. Chen, Y. C. Shin, S. Chatterjee, Y.-C. Tsai, Y. Nishi, R. M. Wallace, and E. Pop, Nano Lett. **19**, 6352 (2019).
[20] A. Ortiz-Conde, F. J. García Sánchez, J. J. Liou, A. Cerdeira, M. Estrada, and Y. Yue, Microelectron. Reliab. **42**, 583 (2002).
[21] B. Chamlagain, Q. Li, N. J. Ghimire, H.-J. Chuang, M. M. Perera, H. Tu, Y. Xu, M. Pan, D. Xaio, J. Yan, D. Mandrus, and Z. Zhou, ACS Nano **8**, 5079 (2014).
[22] H. Ji, G. Lee, M. K. Joo, Y. Yun, H. Yi, J. H. Park, D. Suh, and S. C. Lim, Appl. Phys. Lett. **110**, 183501 (2017).
[23] M. Hosseini, M. Elahi, M. Pourfath, and D. Esseni, J. Phys. D: Appl. Phys. **48**, 375104 (2015).
[24] D. Esseni, P. Palestri, and L. Selmi, *Nanoscale MOS Transistors: Semi-Classical Transport and Applications* (Cambridge University Press, Cambridge, 2011).
[25] A. Paussa and D. Esseni, J. Appl. Phys. **113**, 93702 (2013).
[26] M. Hosseini, M. Elahi, M. Pourfath, and D. Esseni, IEEE Trans. Electron Devices **62**, 3192 (2015).
[27] Z.-Y. Ong and M. V. Fischetti, Phys. Rev. B **88**, 45405 (2013).
[28] A. Singh, J. Appl. Phys. **45**, 1908 (1974).
[29] Y. Namba, Jpn. J. Appl. Phys., Part 1 **9**, 1326 (1970).
[30] D. S. Campbell and A. R. Morley, Rep. Prog. Phys. **34**, 283 (1971).
[31] C. J. McClellan, E. Yalon, K. K. H. Smithe, S. V. Suryavanshi, and E. Pop, in 75th Annual Device Research Conference (2017), pp. 1–2.
[32] L. Cai, C. J. McClellan, A. L. Koh, H. Li, E. Yalon, E. Pop, and X. Zheng, Nano Lett. **17**, 3854 (2017).
[33] A. Rai, A. Valsaraj, H. C. P. Movva, A. Roy, R. Ghosh, S. Sonde, S. Kang, J. Chang, T. Trivedi, R. Dey, S. Guchhait, S. Larentis, L. F. Register, E. Tutuc, and S. K. Banerjee, Nano Lett. **15**, 4329 (2015).
[34] S. V. Suryavanshi, A. J. Gabourie, A. Barati Farimani, and E. Pop, J. Appl. Phys. **126**, 55107 (2019).
[35] M. Malits, I. Brouk, and Y. Nemirovsky, Sensors **18**, 1629 (2018).
[36] R. Caverly, G. Hiller, D. Rancour, J. Bukowski, and Z.-W. Tang, Solid State Electron. **38**, 1879 (1995).
[37] E. Yalon, Ö. B. Aslan, K. K. H. Smithe, C. J. McClellan, S. V. Suryavanshi, F. Xiong, A. Sood, C. M. Neumann, X. Xu, K. E. Goodson, T. F. Heinz, and E. Pop, ACS Appl. Mater. Interfaces **9**, 43013 (2017).

Published under license by AIP Publishing

[38]K. M. Razeeb, E. Dalton, G. L. W. Cross, and A. J. Robinson, Int. Mater. Rev. **63**, 1 (2018).
[39]R. Suri, A. P. Thakoor, and K. L. Chopra, J. Appl. Phys. **46**, 2574 (1975).
[40]W. F. Leonard and R. L. Ramey, J. Appl. Phys. **37**, 3634 (1966).
[41]J. W. C. Vries, Thin Solid Films **167**, 25 (1988).
[42]S. M. Shivaprasad and M. A. Angadi, J. Phys. D: Appl. Phys. **13**, L171 (1980).
[43]M. M. Rojo, Z. Li, C. Sievers, A. C. Bornstein, E. Yalon, S. Deshmukh, S. Vaziri, M. H. Bae, F. Xiong, D. Donadio, and E. Pop, 2D Mater. **6**, 011005 (2018).
[44]R. B. Belser and W. H. Hicklin, J. Appl. Phys. **30**, 313 (1959).
[45]H. Marom and M. Eizenberg, J. Appl. Phys. **96**, 3319 (2004).
[46]F. Warkusz, J. Phys. D: Appl. Phys. **11**, 689 (1978).
[47]K. L. Chopra and L. C. Bobb, Acta Metall. **12**, 807 (1964).
[48]A. Kumar, G. Chandra, and O. P. Katyal, J. Mater. Sci. **23**, 2361 (1988).

Published under license by AIP Publishing